communications earth & environment

Article

https://doi.org/10.1038/s43247-024-01345-3

Microbial communities modulate chemical weathering and carbon dioxide cycling in an active orogen in Taiwan

Check for updates

Pei-Ling Wang[1,2,10] ✉, Tzu-Hsuan Tu[3,4,10] ✉, Li-Hung Lin[2,4,10], Hsi-Ling Chou[4], Yi-Jie Wang[1], Jhen-Nien Chen[4], Lu-Yu Wang[4], Jui-Ming Chang[4,5], Mei-Fei Chu[4], Yi-Chun Hsu[6], Chung-Pai Chang[6], Yih-Ming Wu[2,4,7], Yen-Tsu Lin[8] & Chien-Chung Ke[9]

Chemical weathering modulates carbon transfer between the crust, hydrosphere, and atmosphere. The extent to which microbial processes are involved in mineral dissolution remains elusive. Here, we performed geochemical and molecular analyses of river water and other materials collected from a rapidly exhuming catchment in eastern Taiwan. In addition to solute generation driven primarily by pyrite-induced carbonate weathering, highly skewed microbial community compositions with abundant *Sulfuricurvum* and *Thiobacillus* members were detected during high-water periods. The yields of these taxa were also correlated with those of sulfate and sediments, suggesting that pyrite oxidation and carbonate dissolution were facilitated by sulfur-respiring microorganisms inhabiting erodible materials at a pace comparable to the supply of sulfur-bearing minerals through rapid exhumation. The net CO_2 export regulated by such potentially supply-limited, microbially-mediated mineral weathering greatly surpasses the global average, highlighting active orogens in high-standing islands as important CO_2 contributors rendered by tandem biotic and abiotic processes.

Chemical weathering of silicate minerals has conventionally been treated as the most effective abiotic sink for atmospheric CO_2[1]. While the fluxes of photosynthesis and respiration are nearly balanced[2], the removal of atmospheric CO_2 through silicate weathering in line with the burial of biospheric carbon in major river systems can offset a considerable portion of the CO_2 emitted from geological sources (e.g., volcanic and metamorphic degassing), thereby regulating climatic fluctuations over geological time scales[3]. However, weathering of geological materials does not necessarily lead to carbon sequestration but instead contributes to intensifying CO_2 emissions (e.g., pyrite-induced carbonate dissolution and oxidation of petrogenic organic carbon)[4,5]. Growing evidence has shown that pyrite oxidation is much more prevalent than previously thought[5,6]. Based on the solute contents and sulfur isotopic compositions of sulfate, the model calculation estimates that the export of pyrite-derived sulfate from major rivers could reach 1.3×10^{12} moles yr^{-1}, a quantity comparable to the solute budget of silicate weathering[7]. As sulfuric acid dissolves carbonate minerals more rapidly than carbonic acid, this reaction leads to a net release of CO_2 gas at a time scale of less than 10^7 yrs[8], thereby counteracting the removal of CO_2 by silicate weathering[5].

Pyrite-induced carbonate weathering could have been even more effective than silicate weathering in tectonically active terranes[9]. This inference is readily illustrated in previous studies on catchments distributed in the Himalayas, Andes, New Zealand, and Taiwan orogens[9–13]. The area-specific flux of pyrite-induced carbonate weathering in these active mountain belts has been estimated to reach a level (millions of moles km^{-2} yr^{-1}) several orders of magnitude greater than that in major river basins (see review and compilation in ref. 1). This pattern has been attributed to the enhanced exposure of fine-grained pyrite and rock fragments to rain and groundwater infiltrating through the pore space and fracture of talus deposits and bedrock, a process aided by rapid

[1]Institute of Oceanography, National Taiwan University, Taipei 106, Taiwan. [2]NTU Research Center for Future Earth, National Taiwan University, Taipei 106, Taiwan. [3]Department of Oceanography, National Sun Yat-sen University, Kaohsiung 804, Taiwan. [4]Department of Geosciences, National Taiwan University, Taipei 106, Taiwan. [5]Disaster Prevention and Water Environment Research Center, National Yang Ming Chiao Tung University, Hsinchu 300, Taiwan. [6]Center of Space and Remote Sensing Research, National Central University, Taoyuan 320, Taiwan. [7]Institute of Earth Sciences, Academia Sinica, Taipei 115, Taiwan. [8]Geological Resources Division, Central Geological Survey, Ministry of Economic Affairs, New Taipei City 235, Taiwan. [9]Advanced Geological Research Task Force, Sinotech Engineering Consultants, Inc., Taipei 114, Taiwan. [10]These authors contributed equally: Pei-Ling Wang, Tzu-Hsuan Tu, Li-Hung Lin. ✉e-mail: plwang@ntu.edu.tw; thtu@mail.nsysu.edu.tw

fluvial incision and hillslope mass wasting associated with rapid tectonic uplift[12,14].

Microbial catalysis has been speculated to contribute to the production of sulfuric acid from pyrite in orogenic belts[1]. However, the potential niche and community assemblage, and the extent to which microbial sulfur respiration is involved remains largely unknown. Addressing such a knowledge gap can provide a basis to unveil how the weathering thermostat of climatic feedback is regulated by and co-evolves with microbially acid production. In this study, we aimed to determine the potential microbial role in pyrite-induced chemical weathering in a rapidly exhuming catchment of eastern Taiwan. Field campaigns were conducted between 2016 and 2018 to sample and analyze river water, sediments in benthic zones, short-path creeks, groundwater, hot springs, soils, and rocks from the Hsin-Wu-Lu River headwaters of the Bei-Nan catchment (Fig. 1). The catchment was chosen by taking the advantage that the bedrock mainly composed of slate, greenschist, and blackschist is rapidly exposed to the surface environment (several to tens of mm yr^{-1}, depending on the time scale[15–18]) by tectonic uplift and accompanying river incision and mass wasting, providing vast amounts of reactive pyrite for mineral weathering. The catchment is also characterized by the export of high suspended particulates to the ocean at a flux (20–88 Mt yr^{-1} or 0.013–0.055 Mt km^{-2} yr^{-1})[19,20] ranking among the highest in Taiwan. Spatial and temporal variabilities in chemical weathering and microbial community across the catchment were examined to resolve the relationships between hydrological and microbial shifts imposed by event-driven erosion.

Results and discussions

Pyrite-induced chemical weathering in an active orogen

Analyses of 102 river water samples yielded that Ca^{2+}, SO_4^{2-}, and dissolved inorganic carbon (DIC) were the main solute constituents (Supplementary Table S1). After correcting for rain inputs, the plot of Ca^{2+}/Na^+ against Mg^{2+}/Na^+ revealed that most samples clustered around an end member represented by carbonate minerals rather than silicate minerals (Supplementary Fig. S1; detailed correction in Supplementary Methods). The predominance of carbonate over silicate weathering was further quantified using a Bayesian approach for the mass balance configured by the model compositions of silicate and carbonate minerals (Supplementary Methods). The results indicated that carbonate weathering produced >90% of the total cation yields in most tributaries (HLBS, LD, and MLL02) and the main stem (CWL01 and 04), regardless of the sampling time (Fig. 1 and Supplementary Figs. S2 and S3).

The only exception occurs for DL (Da-Lun River), along which hot fluids are discharged from a cluster of springs identified 15 km upstream from the confluence with the Hsin-Wu-Lu River. These hot fluids were enriched in Na^+ and DIC (Supplementary Table S1), a geochemical pattern modulated primarily by water-rock interactions at high temperatures

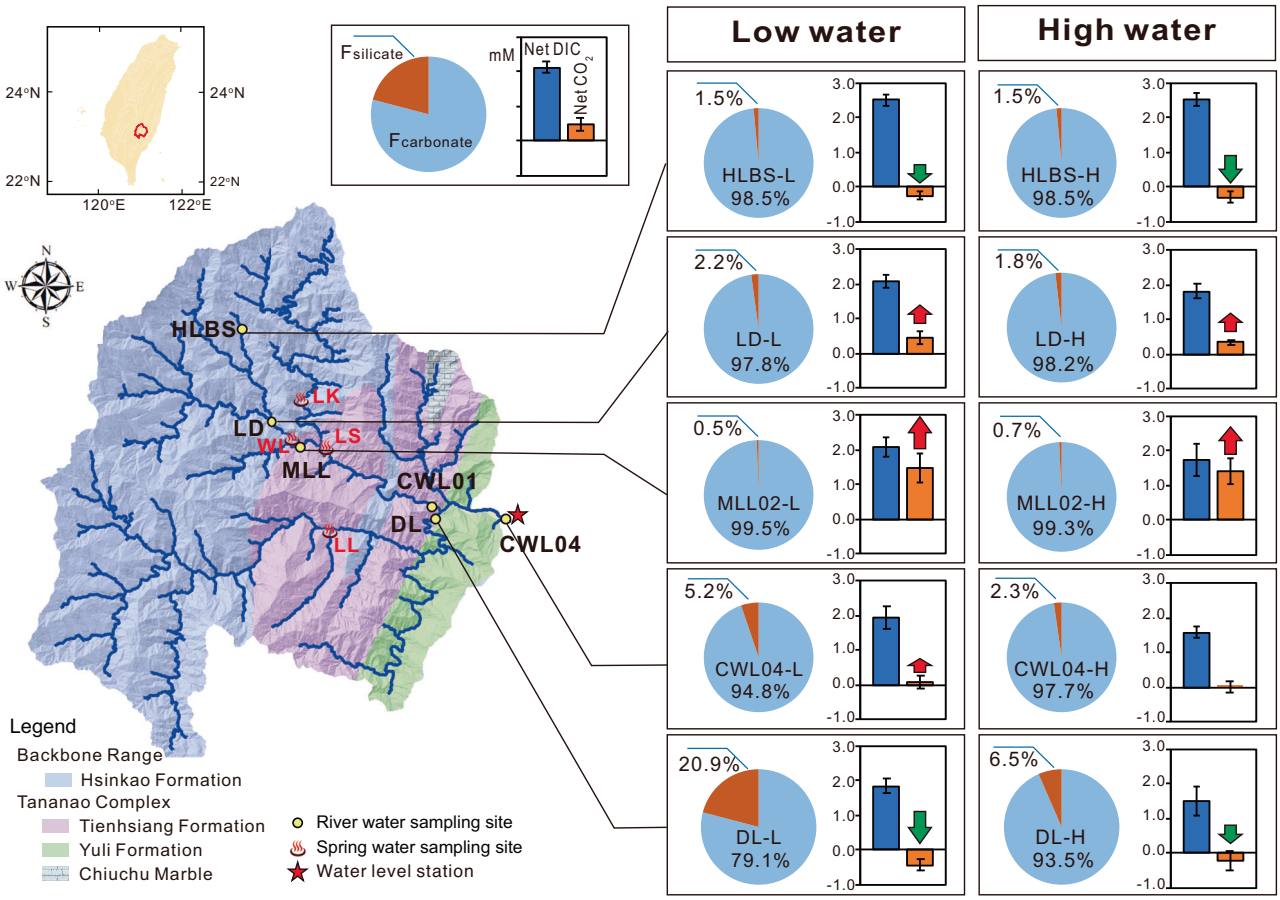

Fig. 1 | Geological map of the study area overlaid with sampling locations, the contributions of weathering pathways to the solute production, the net DIC production, and the transient CO_2 gas emission. The relative fractions of cations from silicate and carbonate weathering were calculated from the data set corrected for precipitation and hot spring inputs using a Bayesian algorithm based on the modeled compositions of silicate and carbonate minerals. The fractions of the solute loads from individual pathways were further deconvoluted to constrain the acid contribution and bulk CO_2 production considering the charge balance for reactions that produce both DIC and gaseous CO_2 (Supplementary Methods). The fraction of each pathway ("F" value) represents an average for the high-water or low-water periods (sample names attached with "-H" and "-L", respectively). The net DIC production represents the production of DIC from carbonate dissolution. For comparison, the transient CO_2 emission is derived from the subtraction of the gaseous CO_2 produced from carbonate dissolution from the dissolution of atmospheric CO_2. The red and green arrows mark the net transient emission and sink of gaseous CO_2, respectively. The error bars represent one standard deviation. Detailed computation approaches can be found in Supplementary Methods.

(<12% of cations in DL water originated from high-temperature reactions). By subtracting this hot-spring component, the DL solute pattern revealed that carbonate weathering contributed 93 ± 6% and 79 ± 8% of the total cation yields during the high- and low-water periods, respectively (Fig. 1 and Supplementary Figs. S2 and S3).

The capacity of carbonate minerals to buffer pyrite-derived acids appears to be insufficient to accommodate the production of DIC for most tributaries and the main stem, as evidenced by the $(Ca^{2+} + Mg^{2+})$/sulfate ratios between one and two (Fig. 2a; except for some samples from HLBS, DL, and CWL04). The stoichiometric disproportionation suggests that pyrite-induced carbonate weathering can lead to the formation of both bicarbonate and CO_2 gas. With a approach considering the charge balance, the net emission of gaseous CO_2 occurred in all periods for LD, MLL02, and CWL01, and in some periods for CWL04 (Supplementary Methods). In contrast, the net removal of atmospheric CO_2 occurred in all periods for HLBS and DL, and some periods for CWL04, and was associated with the lower sulfate (0.5–1.3 mM for HLBS and DL versus >2 mM for other tributaries) and comparable concentrations of divalent ions and DIC. The derived net CO_2 directivity does not incorporate the CO_2 emissions associated with the export of riverine DIC into the ocean (Fig. 1) and the subsequent precipitation of carbonate minerals over geological time, thereby representing a transient status for the CO_2 cycle.

The predominance of pyrite-driven carbonate weathering on solute export is supported by the isotopic composition of sulfate (Fig. 2b; Supplementary Notes 1). The $\delta^{34}S$ and $\delta^{18}O$ values of sulfate ranged from −12 to +3 ‰ and from −8 to +4 ‰, respectively. Such a wide range of $\delta^{34}S$ values and their distinction from marine sulfate composition (+10 to +35‰)[21] suggest that sulfur in sulfate is not sourced from marine evaporites but rather from reduced sulfur that experienced diagenesis and subsequent metamorphism. On the other hand, the $\delta^{18}O$ values reflect the mixed source compositions of oxygen (atmospherically derived oxygen of +23.8‰ and water-derived oxygen between −16 and −10‰; Supplementary Fig. S4). The mass balance calculation showed that water contributed >50% of oxygen in sulfate for all samples (Fig. 2c; Supplementary Note 1). For some samples from the tributary (HLBS) located farthest upstream, the contribution of water-derived oxygen dominated over the atmospherically derived oxygen at a much greater level (>90%; Fig. 2c). Both ferrihydrite and atmospheric oxygen are important oxidants to drive the production of sulfuric acid. Considering the sluggish reactivity of pyrite oxidation under ambient conditions[22,23], microbial enzymatic catalysis with or without oxygen may account for copious sulfate production in the investigated catchment.

Microbial role in pyrite oxidation

Analyses of 16S rRNA gene amplicons yielded diverse community compositions (Fig. 3). These amplicon sequence variants (ASVs) were phylogenetically assigned to 88 phyla across Bacteria (74) and Archaea (14) domains. While 30,765 ASVs were recovered, soil communities appeared to be the most diverse among all habitats (Supplementary Tables S2 and S3). For river water and sediments, the diversity indices for high-water periods were lower than those for low-water periods ($p < 0.05$, Dunn's test; Supplementary Tables S2 and S3, and Supplementary Fig. S5). Higher percentages of ASVs (> 10%) were shared between the water and sediment communities than between the soil and water/sediment communities (Supplementary Fig. S6). Among the diverse community members, ASVs closely affiliated with two genera, *Sulfuricurvum* within Campylobacteria and *Thiobacillus* within Gammaproteobacteria, were particularly abundant in the high-water samples. The proportions of these two genera ranged from 1% to 79% and from 3% to 36% of the reads, respectively (Fig. 3a, b; Supplementary Table S4). The summed proportions were greater than 40% in 23 of the 29 samples. Comparable results were obtained from benthic sediments (summed proportions from 24% to 74% of the reads; Supplementary Table S4). In contrast, these two genera were much less abundant (<11% in total) in the majority of the low-water river and sediment samples (17 out of 21 samples; exceptions were some samples collected in May 2017) and in short-path creeks, groundwater, hot springs, soils, and rocks. Instead, Acidobacteriota, Actinobacteriota, Alphaproteobacteria, Bacteroidota, Cyanobacteria, and Gammaproteobacteria constituted the main classes or phyla (Fig. 3a). The contrasting proportions of these two genera between water levels were further supported by quantitative PCR (qPCR) results (Fig. 4). Their 16S rRNA gene copies ranged between 3×10^5 and 3×10^8 copies L^{-1} for the high-water samples, and were generally greater than those for the low-water samples (from below detection to 1×10^8 copies L^{-1}; $p < 0.05$, Dunn's test; Supplementary Table S4). The gene copies also varied positively with the sediment concentrations (Supplementary Fig. S7) and sequence proportions (Supplementary Fig. S8). By multiplying the measured characteristics with the discharges, the annual yields of these two taxa were found to be highly correlated with those of sediment and sulfate ($\rho > 0.6$ and $p < 0.0001$; Fig. 4; Supplementary Note 2). Finally, two of the metagenome assembled genomes (MAGs) recovered (Supplementary Note 2, Supplementary Figs. S9 and S10, and Supplementary Table S5) contained a suite of genes affiliated with *Sulfuricurvum* and *Thiobacillus* related strains capable of autotrophically metabolizing reduced sulfur under low-oxygen conditions (for *Sulfuricurvum*) or variable oxygen levels (for *Thiobacillus*)[24,25].

The sequence resemblance with the *Sulfuricurvum* and *Thiobacillus* affiliated strains (Supplementary Fig. S9), the community variation and functional pattern correlated with the water level and sediment concentration (Figs. 3 and 4, and Supplementary Figs. S7 and S10), and the correlation between the yields of target taxa, sediment, and sulfate (Fig. 4) provide important implications for the microbial role, capacity, and niche in pyrite oxidation. First, these sulfur oxidizers were intimately associated with sediments, suggesting that surface and near-surface environments with erodible materials, such as talus deposits on the hillslope, sediments temporally piled in the bank, or fractured bedrock on the channel wall or as part of the riverbed, would be the most plausible niches for the proliferation of these two genera. Second, these data patterns support the likelihood that the target sulfur-respiring taxa actively oxidized reduced sulfur. The oxidation product, sulfate, along with the solutes derived from weathering processes, could have accumulated in either the pore space of talus deposits and bank sediments or fracture bedrock and migrated toward the river in accordance with hydraulic gradients. Over a period impacted by typhoons or torrential rains, talus deposits, bank sediments, or fractured bedrock are rapidly recharged and saturated with groundwater, becoming highly conductive to groundwater transport[14,26,27]. In particular, the erodible materials are destabilized by either the failure of the slope base undermined by the turbulent flow or the reduced cohesion associated with the saturation of pore space[28], thereby draining the sediment-bound communities into the river. As a result, the taxon yields along with sulfate yields recovered from river water were highly dependent on the amount of sediment or material entrained by high-water events (Fig. 4). During low-water periods, the solute dilution caused by the torrential runoff is essentially absent[29,30] Therefore, the groundwater sulfate would constitute a substantial portion of river sulfate when compared with high-water periods. By contrast, only trace amounts of sediment-bound taxa or sessile populations were released into the river through shallow and deep groundwater circulation. Therefore, the river communities would be primarily composed of members that loosely colonized the surface of rocks and sediments exposed to the river water.

Weathering in deep subsurface environments can be a potential contributor to the solute budget during low-water periods. The assertion is supported by nearly coeval variations in precipitation, groundwater level, and river discharge particularly for the extreme events (Supplementary Fig. S11), and elevated sulfate concentrations (~9 mM) of groundwater in a 100-m deep borehole located at ~30 m from river DL (Supplementary Table S1). The observed groundwater is likely connected to the riverbed through the fracture network extended from the subsurface beneath the hillslope, channeling subsurface sulfate to the river water. One notable feature is that the abundances of potential sulfur oxidizers in groundwater were drastically lower (0.91%) than those in river water during high-water periods (Supplementary Fig. S12), which seems to contradict microbially

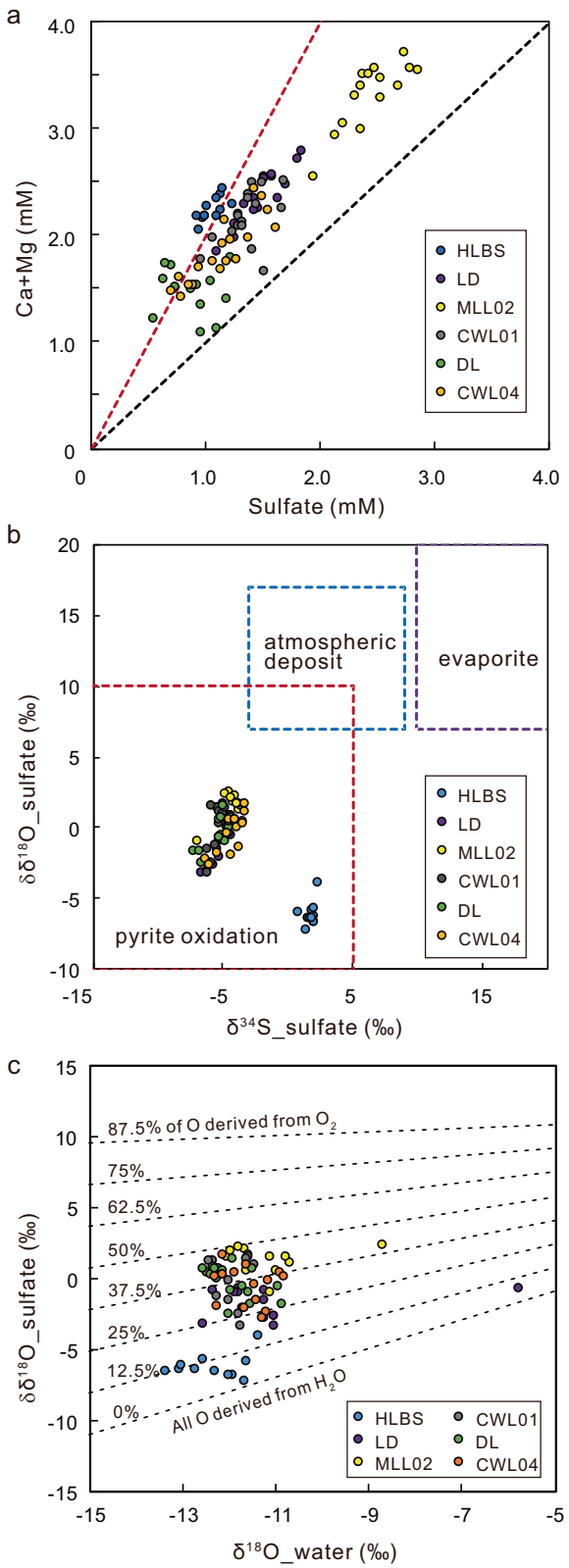

Fig. 2 | Sulfate abundances and isotopic compositions of river water. Plots of **a** (Ca^{2+}+Mg^{2+}) versus sulfate concentrations, **b** sulfur versus oxygen isotopic compositions of sulfate, and **c** oxygen isotopic compositions of sulfate versus of water. Dashed lines with slopes of 1 and 2 in **a** represent carbonate weathering by sulfuric acid with the production of DIC (Eq. (S10) in Supplementary Methods) and gas CO_2 (Eq. (S11) in Supplementary Methods), respectively. Isotopic compositions of sulfate from seawater (or evaporite), pyrite originally from microbial sulfate reduction during early diagenesis, and atmospheric deposits are plotted for comparison in **b**. The dashed lines in **c** represent the source contribution for oxygen in sulfate produced by pyrite oxidation with oxygen incorporated from the atmospheric oxygen or the water molecule. Detailed modeling approaches are described in Supplementary Note 1.

mediated pyrite oxidation. A plausible explanation for such an apparent discrepancy is that these sulfur oxidizers might have colonized the fracture surface, actively converting sulfur to sulfuric acid for energy conservation. This scenario might be intuitively valid because pyrite is visible and prevalent in bank sediments, slate, and schist. The direct contact between sulfur-respiring microorganisms and pyrite surface enables to harness metabolic energy and facilitate electron transfer more efficient potentially through electron carrier or nanowire postulated for extracellular electron transfer during the iron reduction[31]. Previous studies have also suggested that the abundance of sessile communities in the subsurface can range up to 1000 times higher than those of planktonic communities[32]. If so, these attached sulfur oxidizers can still produce elevated sulfate, impacting downstream carbonate weathering and other biogeochemical cycling while being exempted from detection through current sample retrieval. Abiotic pyrite oxidation previously reported for shales with small pore throats was noted and discussed[33] (Supplementary Discussion).

High chemical flux and CO_2 emission in small mountainous catchments

Based on conservative decadal discharge estimates, the mountainous catchment drained by the investigated river in eastern Taiwan exported a total of $1.5 \pm 0.3 \times 10^9$ moles yr^{-1} sulfate downstream through chemical weathering (Supplementary Discussion). Such a quantity is comparable with the export from the Gao-Ping River in southern Taiwan (7.8×10^9 mole yr^{-1}) and the Li-Wu River in eastern Taiwan ($7.8–9.3 \times 10^8$ mole yr^{-1})[1,11,14]. The combined export of sulfate from these three catchments with an area of 4331 km^2 (0.003% of the global catchment area) results in a total yield of ~1.1×10^{10} moles yr^{-1}, which represents 0.85% of the global riverine pyrite-induced sulfate[7], and an area-specific flux of 2.5×10^6 moles km^{-2} yr^{-1}. While the area-normalized flux surpasses the global average by two to three orders of magnitude[7], the yield of riverine sulfate is comparable to the amount of sulfur in bedrock (1.6×10^{10} moles yr^{-1}; Supplementary Discussion) exposed through rapid exhumation and erosion by channel incision and mass wasting[16]. Therefore, the high fluxes represent the outcome of intensive carbonate weathering driven by pyrite oxidation, which is potentially mediated by *Sulfuricurvum* and *Thiobacillus* members at a pace consistent with the exposure of fresh bedrock. The estimates also suggest that microbially driven chemical weathering is supply-limited, converting nearly all exhumed sulfur minerals to soluble sulfate prior to export to the ocean. Furthermore, where the localized acid production exceeds the buffering capacity of carbonate minerals, the intimate microbe-mineral association enables the net, transient emission of gaseous CO_2 and produces an overwhelmingly large quantity of DIC, which could ultimately lead to net CO_2 generation over geological time scales (Fig. 1). The exported DIC flux-from mineral weathering was calculated to be 2.8×10^9 moles yr^{-1} (Supplementary Discussion), which is equivalent to 1.4×10^9 moles C yr^{-1}, or 1.7×10^4 tons C yr^{-1}, or 27 tons C km^{-2} yr^{-1} emission of CO_2. Nevertheless, the derived conservative CO_2 fluxes are either comparable to or greater than the net CO_2 fluxes of mineral weathering, export from the oxidation of petrogenic carbon, and sequestration by the burial of biospheric carbon for catchments in Taiwan[1,34–36], and exceed the values observed for most catchments around the world by up to orders of magnitude (except for site Laval[37]; see compilation in ref. 1). The investigated catchment represents a hotspot of CO_2 emissions potentially rendered by microbe-hydrology-rock interactions in the context of active orogenesis. Finally, high-standing islands around the Pacific Ocean, which constitute only ~3% of the landmass and are prone to convergent tectonics and the impact of meteorological extremes, are estimated to export up to 35% of global sediment flux[20,38].

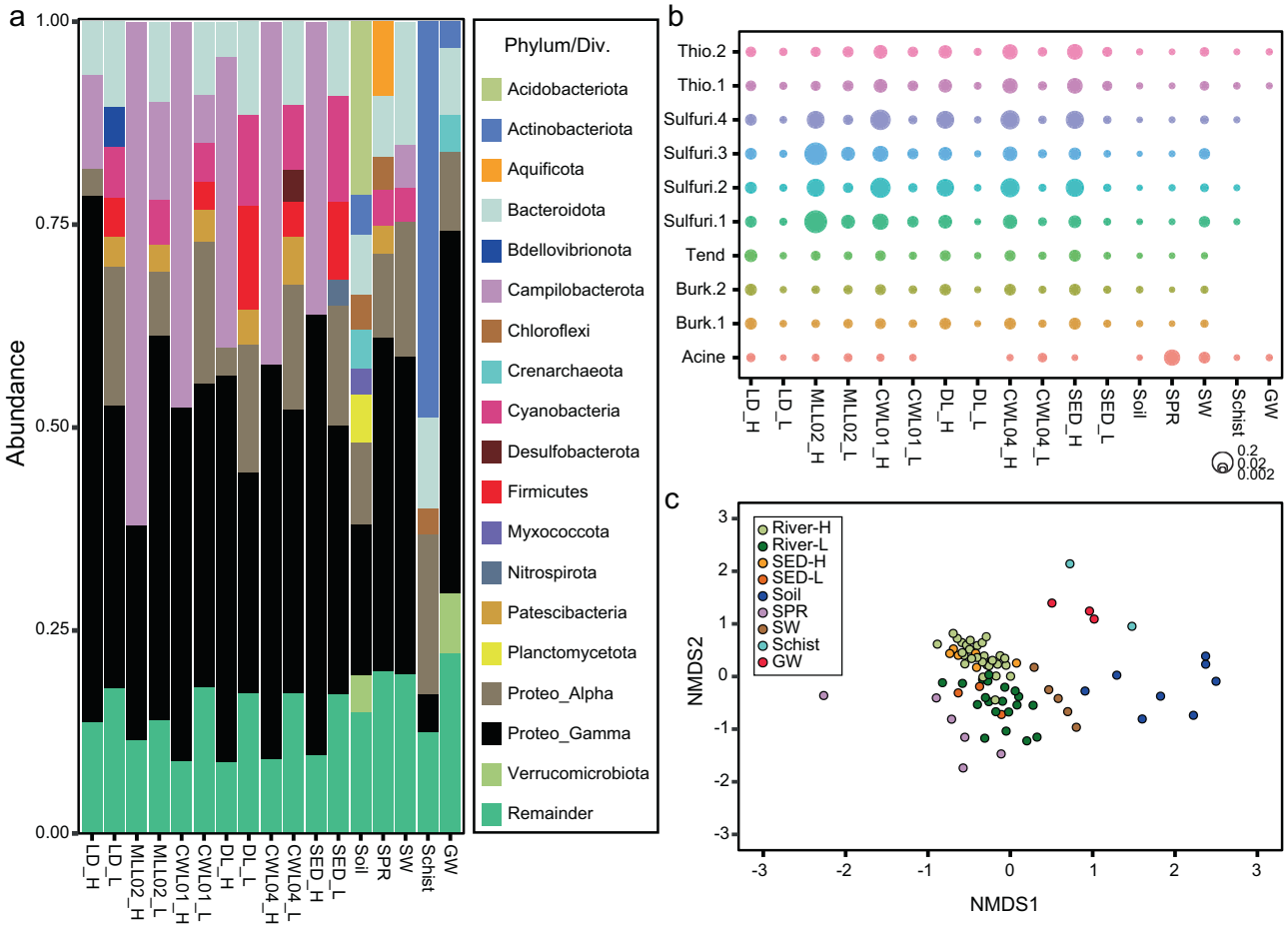

Fig. 3 | Community compositions and variance based on 16S rRNA genes for samples collected from rivers, sediments, short-path creeks, groundwater, hot springs, soils, and schists. a Abundances of major taxonomic units (phyla and classes with >3% read proportions), **b** abundances and taxonomic affiliations of the top 10 most abundant ASVs, and **c** community variance based on the Bray-Curtis distance ordinated by the non-metric multidimensional scaling (NMDS) approach. Sample affiliations were expressed as either site for river water (LD, MLL02, CWL01, DL, and CWL04) or sample category ("SED" for sediment, "SPR" for hot spring, "GW" for groundwater, "SW" for short path creek, and "Schist" for rock). Samples of rivers and sediments were further categorized with "-H" for the high-water level, and "-L" for the low-water level. Scaled circles in **b** represent the read proportions of specific ASVs. Abbreviations for taxonomic units in **b** include "Thio" for *Thiobacillus*, "Sulfuri" for *Sulfuricurvum*, "Tend" for Candidatus *Tenderia*, Burk" for Burkholderiaceae, and "Acine" for Acinetobacter.

While microbial pyrite oxidation is likely sediment-bound, the quantitative extrapolation of the current results to other analogous high-standing islands could be valid only if a transfer function that connects the yields of sulfur oxidizers, sediments, and microbial sulfate is established, tested, and generalized. An extra consideration of sediment residence time would be even more vital when applying this to river systems with wider riparian zones and floodplains. In summary, this study presents a conceptual framework and modern analog to examine whether the engagement of microbial roles in mineral weathering and elemental cycling in global mountain belts is as prevalent and significant, as observed in this study, either on a contemporary time scale or over the geological past.

Methods

Site background and sampling

Taiwan is located at the boundary juxtaposing the Eurasian and Philippine Sea Plates. The northwestward subduction of the Philippine Sea Plate has led to an oblique collision between the Luzon arc and the Eurasian Plate since five million years ago, driving the southward and westward propagation of uplift and exhumation across the island[39]. Rapid uplift exposes various grades of metamorphic rocks above sea level and enables the formation of deeply incised rivers oriented by structural configuration[40]. Among numerous river systems in Taiwan, the Bei-Nan River is selected as the study target because of its high sediment export (20–88 million metric ton yr^{-1})[19,20], uplift and erosion rates (3–15 mm yr^{-1} depending on the time scale)[16,41], and the limited impact of human activity. The study catchment, drained by the Hsin-Wu-Lu River and its tributaries, constitutes the upstream part of the Bei-Nan catchment (Fig. 1), and spans an elevation change between 200 and 2900 m above sea level and an area of 639 km^2. The bedrock classified as the Backbone Range is composed of the Hsinkao Formation (slate belt) to the west and the Tananao Complex (schist belt) to the east[42] (Fig. 1). While the Hsinkao Formation consists mainly of slate/phyllite[43] (Fig. 1b), the Tananao Complex is composed of blackschist, light-colored mica schist, greenschist, and minor marble and metasandstone. Major mineral constituents of either slate or schist include quartz, mica, and plagioclase (±chlorite and graphite)[43]. The peak metamorphic temperatures of the schist and slate belts have been estimated to be 550–580 °C and 450 °C, respectively[42,44–46]. A metagranite body in contact with schist and marble is distributed approximately 15 km upstream of the Da-Lun River[47]. The mineral constituents of the metagranite include quartz, K-feldspar, and plagioclase, with minor amounts of garnet, biotite, zircon, apatite, and pyrrhotite. U-Pb dating on zircon yields ages of ~200 Ma, suggesting arc magmatism related to the subduction of the paleo-Pacific plate. The intrusive body was further rifted from the South China Block during Eocene – Miocene, and accreted into the Tananao Complex by subduction and collision since Miocene[47]. Talus deposits produced from landslides are distributed in the upstream and midstream regions where

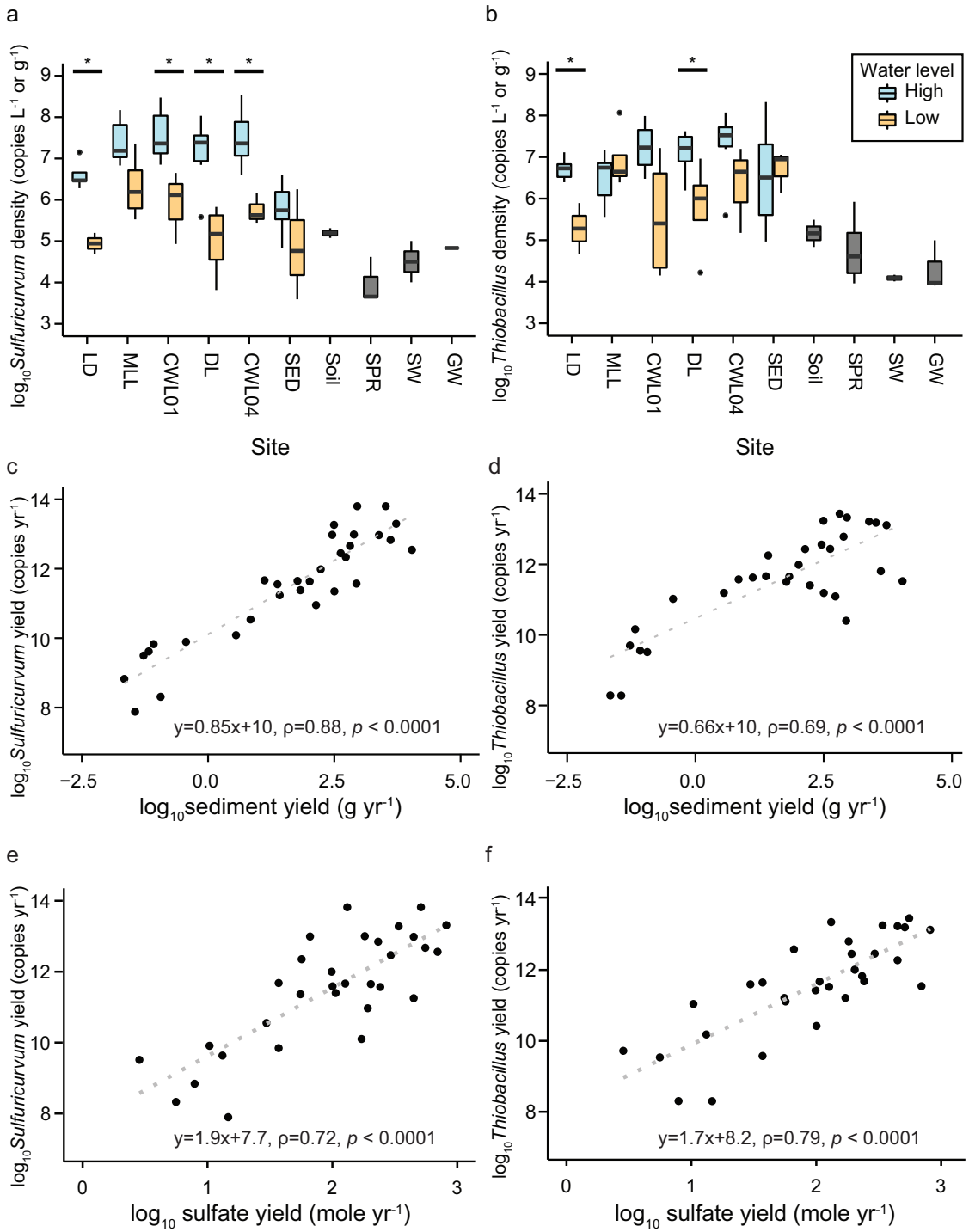

Fig. 4 | Abundances of *Sulfuricurvum* and *Thiobacillus* members and their relationships with the yields of sediment and sulfate. a, **b** qPCR derived 16S rRNA gene copies, and log-log plots for the yields of 16S rRNA gene copies versus sediment (**c**, **d**) and sulfate (**e**, **f**) in river samples. The boxes in **a** and **b** represent the median, and the first and third quartiles of 16S rRNA gene copies for individual specific sites or sample categories. Whiskers represent 1.5 times the interquartile range. Blue and gold boxes are the results for river and sediment samples collected during high- and low-water periods at specific sites, respectively, whereas gray boxes are the results for different categories (abbreviations the same as Fig. 3). Significant differences for abundances between the high-water versus low-water at specific sites are marked by stars (* for $p < 0.05$ by Dunn's test). The yields in **c**–**f** were calculated by multiplying individual parameters with daily discharges that were proportionated from the discharge at CWL04 using the fraction of catchment area (Supplementary Note 2). The discharge during low-water periods (25 cms) was better approximated using the channel width derived from the satellite image and measured flow velocity (Supplementary Note 2).

topographic gradients are high. Soil development is very limited, primarily because of unstable hillslopes and high erosion rates. Hot springs were identified along the Hsin-Wu-Lu River and one of the tributaries, the Da-Lun River (Fig. 1). These hot springs are enriched with bicarbonate, and sodium (Supplementary Table 1) derived from the water-rock interactions at high temperatures. Visual inspection suggests a low discharge of hot fluids from most springs. The only exception was the spring outcrops distributed along the Da-Lun River. Hot fluids at >90 °C were vigorously released from the interface between the metagranite and schists into the river. Therefore, the correction for river chemistry was made particularly for the samples

collected from DL and the downstream section of the Hsin-Wu-Lu River (Supplementary Methods for the detailed correction procedures).

Five main field sites were chosen to cover the major tributaries and possible variations in the chemical characteristics and microbial communities across the catchment. Types of samples include river water from the main stem of the Hsin-Wu-Lu River (sites CWL01 and 04; $n = 18$, respectively) and its tributaries (sites DL, MLL02, LD, and HLBS; $n = 20$, 10, 16, and 12, respectively), sediments in the benthic zone (site DL; $n = 10$), groundwater (near site DL; $n = 3$), hot springs (LL, LS, LK, SM, and WL; $n = 2$, 1, 1, 1, and 1, respectively), short-path creeks ($n = 5$), soils ($n = 8$), schists ($n = 2$), and rainwater (near site LD; $n = 7$). Sample information could be found in Supplementary Table S1. Fieldwork and most sampling activities were conducted between September 2016 and January 2018. The only exception occurred for groundwater collected from a borehole near site DL in September and October of 2018 when the borehole drilled and maintained by the Taiwanese Central Geological Survey was available for this study. Prior to sample collection, some physical characteristics (including temperature, pH, and conductivity) of the water were measured on-site. River water and sediment samples were collected several days after high-water events (typhoons or storms) or during low-water periods (Supplementary Fig. S9). Benthic sediments collected were submerged slightly in river water and distributed near the boundary between the active channel and riparian zone at site DL. They were relatively fine-grained (smaller than the size of coarse sand). The exact depositional age remains unconstrained but is speculated to be on the scale of months as this grain size range is susceptible to mobilization during high-water events. All benthic sediments were collected during the same campaign for sampling of the river water at site DL. Groundwater was collected from a borehole drilled to 100 mbls (meters below land surface) near site DL. The borehole was located approximately 30 meters from the nearby DL River. Groundwater samples were obtained from depth of 67 mbls in September 2018, and 67 mbls and 85 mbls in October 2018. The depth range was used to represent the groundwater from the screen opening at two depth intervals: 64–67 mbls and 88–97 mbls. Rainwater was collected whenever possible. All the other types of samples were retrieved from specific sites once during the investigation period. The attribution of samples to either the high- or low-water period is not straightforward because the water level represents the cumulative effect of precipitation, runoff, groundwater, and events (such as typhoons, monsoons, and storms) that influence the water bodies (Supplementary Fig. S11). Furthermore, the steep topographic variation across the catchment causes rapid variation in water level over an event cycle. Based on field observations, monthly accumulated precipitation, and sediment yield, samples collected in September and October of 2016 (days after typhoons), and June-August and October of 2017 (days after storms) were assigned as high-water samples, whereas the rest were assigned as low-water samples. While most samples were available for geochemical analyses (except that only DNA samples were collected on September 12th, 2016), samples collected on selected dates were used for DNA analyses.

Sample processing

Water samples were filtered using 0.2 μm pore-sized cellulose membranes for different analytical purposes. The particulates on the membranes were frozen in a −20 °C freezer for temporary storage in the field (two days) and in a −80 °C freezer for permanent storage for DNA analyses. Because no additional particulate samples were collected in September and October 2016, wet particulates for DNA analyses were used to infer the sediment concentration. Our in-house test showed that the difference between the dry and wet sediment concentrations was small (<20%) under high sediment conditions (>5 g L^{-1}). Considering that the sediment concentrations of these samples were high (as high as 22 g L^{-1}), wet sediment concentrations were adopted. The filtrates were split into aliquots with or without preservatives for different geochemical analyses. Samples for analyses of isotopic compositions of water were collected by filling polypropylene vials without headspace. Samples for analyses of anion and cation concentrations were collected in polypropylene vials without preservatives and with nitric acid at a final concentration of 2%, respectively. Filtered samples for analyses of isotopic compositions of sulfate were collected in polypropylene bottles, acidified to pH < 4, and preserved with excess $BaCl_2$. Sample processing for DNA and aqueous geochemistry followed similar operational standards and approaches, minimizing the human-induced contamination.

Geochemical analyses

Anions in the filtrates, mainly Cl^- and SO_4^{2-}, were analyzed using an ion chromatograph (ICS-3000, Dionex, USA). Cations were analyzed using an inductive coupled plasma mass spectrometry (ICP-MS-7700, Agilent Technologies, USA). Synthetic and river standards were used to calibrate a range of concentrations (depending on elements). Hydrogen and oxygen isotopic compositions of water were measured using an off-axis integrated cavity output spectroscopy (LGR, USA). Sulfur and oxygen isotopic compositions of sulfate were measured using an isotope ratio mass spectrometry (Delta V advantage or a MAT253, Thermo, Germany) connected with an elemental analyzer (Flash 2000 or EA-Isolink, Thermo, Germany) through which $BaSO_4$ precipitated from the sample was combusted at 900 °C with CuO (for sulfur isotope) and at 1100 °C without oxygen (for oxygen isotope) to generate SO_2 and CO, respectively. The obtained isotopic compositions were expressed as the δ notation referenced to standards [$\delta = (R_{sample}/R_{std} - 1) \times 1000‰$, where R is the ratio of heavy over light isotopes]. Standards include the Vienna Standard Modern Ocean Water (VSMOW) for hydrogen and oxygen isotopes, and Vienna Canyon Diablo Troilite (VCDT) for sulfur isotopes. Certified reference materials were analyzed along with the samples to monitor their precision. The precisions were ±0.2‰ for $\delta^{34}S$ and ±0.4‰ for $\delta^{18}O$ for sulfate by the mass spectrometry measurements, ±0.2‰ for $\delta^{18}O$ and ±2.0‰ for $\delta^{2}H$‰ by the spectroscopy technology.

Molecular analyses

Crude DNA was extracted from filters, sediments, soils, and rock fragments using the PowerSoil DNA Isolation Kit (Qiagen, Germany). A total of 85 DNA extracts were obtained (Supplementary Table S2) and stored at −80 °C for subsequent analyses. Polymerase chain reaction (PCR) amplification was applied to all DNA extracts using the primers F515 (5'–GTG CCA GCM GCC GCG GTA A–3') and R806 (5'–CCC GTC AAT TCM TTT RAG T–3') targeting the V4 region of 16S rRNA genes[48]. The amplicons were checked on gel electrophoresis, purified, and sequenced on an Illumina Miseq platform (Illumina, USA). For metagenomic analyses, two DNA extracts from river water collected at MLL02 and DL in May 2017 were used to construct libraries. An insert size of 200–600 bp and 50 ng of DNA of each sample were prepared using an Ovation Ultralow System V2 1-96 (Nugen Technologies, USA). Paired-end sequencing was performed on an Illumina MiSeq platform. The schemes and reagents used for PCR were the same as those described in refs. 49,50.

Quantitative PCR (qPCR) was used to analyze the copies of 16S rRNA genes for bacteria, and populations related to genera *Sulfuricurvum* and *Thiobacillus* in crude extracts from all sample categories using a MyiQ Real Time PCR Detection System (Bio-Rad, USA) and a QuantStudio 3 Real-Time PCR system (Applied Biosystems, USA). Standard preparations and PCR conditions were the same as those described in refs. 50,51. Primers targeting specific groups included: B27f and EUB338r for bacteria[50], Sucl-650f (5'–CTA GAG TTC AGA AGG GGC–3') and Sucl-839r (5'–GTC ACC GAA AAG ACG AGC–3') for *Sulfuricurvum* (in-house design), and Thio3 (5'–AGT TCA AAA CGC CAT TCC CA–3') and Thio1032 (5'–CCT GTG TTC CGA TTC CCT–3') for *Thiobacillus*[52]. The 16S rRNA gene copies were calculated based on the length of the amplicon, assuming 650 g mol^{-1} for one base pair of DNA.

Amplicon sequence processing

The bioinformatics packages, Mothur ver.1.40.0[53] and QIIME2 ver. 2019.10[54], were used to process the sequence reads. Quality filtering, dechimerization, and inference of amplicon sequence variants (ASVs) were carried out using the "DADA2" plugin in QIIME2[55] with the default

parameters. The classifier was trained using the SILVA 16S rRNA reference database (release 138) with 99% identity[56].

Metagenome assembling

Reads were co-assembled using MEGAHIT (v.1.2.9) with the 'meta-large' preset parameter[57]. Genomic binning was conducted using Metabat 2[58], MaxBin[59], and CONCOCT[60], after which genome refinement was performed using MetaWRAP[61]. The quality of metagenome assembled genomes (MAGs) was measured for the completeness and contamination using CheckM[62] and those MAGs with more than 70% completeness and less than 3% contamination were further analyzed (Supplementary Table S5). Taxonomy for MAGs was assigned using GTDB-tk (v1.3.0), based on the Genome Taxonomy Database[63]. Gene calling was performed using the Prodigal v2.6.3[64] with translation code 11 within the MetaWRAP pipeline. The PROKKA pipeline[65] was used for gene prediction and functional annotation. The sequences of 16S rRNA genes were identified from the MAGs using the 'ssu_finder' tool integrated within CheckM. The abundance of MAGs was calculated with Salmon[66] built in MetaWRAP[67] and expressed as genome copies per million reads.

Abundances of key functional genes in metagenomes

To determine the abundance of genes matching specific metabolic functions, merged and filtered reads were mapped to assembled contigs using bowtie2 with the default settings[68]. The number of reads mapped to open reading frames (ORFs) of defined functions based on annotations of the JGI KEGG Orthology database[67,69,70] were counted. Specific ORFs of interest were manually checked with tablet searches using an e-value cutoff of 10^{-12}. Key metabolic genes were defined according to previously published databases[71,72]. The count of read hits to specific key genes was divided by the average count of read hits to 35 single-copy COGs to normalize the gene abundance for each sample[72,73].

Microbial community analyses

To equalize the sequencing depth for 16S rRNA gene analysis, the read numbers for individual samples were rarefied to 4899 (the lowest sequence number across all samples) through 100 sequence random re-sampling of the original ASV table. The rarefied sequences were used to calculate the alpha diversity indices, including richness (observed-species and Chao1[74]) and evenness (Shannon diversity[75] and ACE[76]), to assess the diversity and completeness of the ASV representation in each sample. For beta diversity, the entire ASV table was normalized using the function cumNorm from the R package metagenomeSeq[77]. A cumulative-sum scaling method was used to calculate the scaling factors equal to the sum of counts up to a particular quantile to normalize the read counts that takes uneven sequencing depth into account[77]. The dissimilarity matrix between samples was computed using the Bray-Curtis method[78], and visualized through the ordination of non-metric multidimensional scaling (NMDS). Permutational multivariate analysis of variance (PERMANOVA) with 1000 permutations was used to identify changes in microbial community structure between water levels or sample categories[79]. All statistical analyses were performed in R using packages ggplot2, phyloseq, and vegan[80–82].

Network analyses

Packages, including *igraph*, *Hmisc*, and *qvalue* libraries in R, were used to construct the co-occurrence network. To reduce the complexity, only ASVs with a proportion of >0.05% across all samples were retained. In this regard, 271 and 276 ASVs from 49 and 63 samples were used for the high- and low-water periods, respectively. The pairwise Spearman's correlation between ASVs was valid with a correlation coefficient $>|0.7|$ and a p value < 0.01 (Benjamini and Hochberg adjusted). Network visualization and modular analysis were conducted using Gephi[83].

Reporting summary

Further information on research design is available in the Nature Portfolio Reporting Summary linked to this article.

Data availability

Geochemical data and sample information are available at Zenodo (https://doi.org/10.5281/zenodo.10608929). Amplicon and metagenome sequences are available through the NCBI SRA (www.ncbi.nlm.nih.gov; BioProject accession number PRJNA894714).

Received: 14 June 2023; Accepted: 26 March 2024;
Published online: 02 April 2024

References

1. Hilton, R. G. & West, A. J. Mountains, erosion and the carbon cycle. *Nat. Rev. Earth Env.* **1**, 284–299 (2020).
2. Schlesinger, W. H. & Bernhardt, E. S. *Biogeochemistry: An Analysis of Global Change*, 4th ed. (Academic Press, 2020).
3. Gernon, T. M. et al. Global chemical weathering dominated by continental arcs since the mid-Palaeozoic. *Nat. Geosci.* **14**, 690–696 (2021).
4. Zondervan, J. R. et al. Rock organic carbon oxidation CO2 release offsets silicate weathering sink. *Nature* **623**, 329–333 (2023).
5. Torres, M. A., West, A. J. & Li, G. Sulphide oxidation and carbonate dissolution as a source of CO_2 over geological timescales. *Nature* **507**, 346–349 (2014).
6. Calmels, D., Gaillardet, J., Brenot, A. & France-Lanord, C. Sustained sulfide oxidation by physical erosion processes in the Mackenzie River basin: Climatic perspectives. *Geology* **35**, 1003–1006 (2007).
7. Burke, A. et al. Sulfur isotopes in rivers: Insights into global weathering budgets, pyrite oxidation, and the modern sulfur cycle. *Earth Planet. Sci. Lett.* **496**, 168–177 (2018).
8. Maffre, P., Swanson-Hysell, N. L. & Goddéris, Y. Limited carbon cycle response to increased sulfide weathering due to oxygen feedback. *Geophys. Res. Lett.* **48**, e2021GL094589 (2021).
9. Torres, M. A. et al. The acid and alkalinity budgets of weathering in the Andes–Amazon system: Insights into the erosional control of global biogeochemical cycles. *Earth Planet. Sci. Lett.* **450**, 381–391 (2016).
10. Blattmann, T. M. et al. Sulphuric acid-mediated weathering on Taiwan buffers geological atmospheric carbon sinks. *Sci. Rep.* **9**, 2945 (2019).
11. Das, A., Chung, C. H. & You, C. F. Disproportionately high rates of sulfide oxidation from mountainous river basins of Taiwan orogeny: Sulfur isotope evidence. *Geophys. Res. Lett.* **39**, L12404 (2012).
12. Emberson, R., Hovius, N., Galy, A. & Marc, O. Chemical weathering in active mountain belts controlled by stochastic bedrock landsliding. *Nat. Geosci.* **9**, 42–45 (2016).
13. Kemeny, P. C. et al. Sulfate sulfur isotopes and major ion chemistry reveal that pyrite oxidation counteracts CO_2 drawdown from silicate weathering in the Langtang-Trisuli-Narayani River system, Nepal Himalaya. *Geochim. Cosmochim. Acta* **294**, 43–69 (2021).
14. Calmels, D. et al. Contribution of deep groundwater to the weathering budget in a rapidly eroding mountain belt, Taiwan. *Earth Planet. Sci. Lett.* **303**, 48–58 (2011).
15. Hsu, Y.-J. et al. Detecting rock uplift across southern Taiwan mountain belt by integrated GPS and leveling data. *Tectonophysics* **744**, 275–284 (2018).
16. Chen, C.-Y., Willett, S. D., Christl, M. & Shyu, J. B. H. Drainage basin dynamics during the transition from early to mature orogeny in Southern Taiwan. *Earth Planet. Sci. Lett.* **562**, 116874 (2021).
17. Kirstein, L. A. et al. Pliocene onset of rapid exhumation in Taiwan during arc–continent collision: new insights from detrital thermochronometry. *Basin Res.* **22**, 270–285 (2010).
18. Lee, Y.-H. et al. Out of sequence faulting in the backbone range, Taiwan: Implications for thickening and exhumation processes. *Earth Planet. Sci. Lett.* **594**, 117711 (2022).
19. Dadson, S. J. et al. Links between erosion, runoff variability and seismicity in the Taiwan orogen. *Nature* **426**, 648–651 (2003).

20. Kao, S. J. & Milliman, J. D. Water and sediment discharge from small mountainous rivers, Taiwan: The roles of lithology, episodic events, and human activities. *J. Geol.* **116**, 431–448 (2008).
21. Claypool, G. E. et al. The age curves of sulfur and oxygen isotopes in marine sulfate and their mutual interpretation. *Chem. Geol.* **28**, 199–260 (1980).
22. Moses, C. O., Nordstrom, D. K., Herman, J. S. & Mills, A. L. Aqueous pyrite oxidation by dissolved-oxygen and by ferric iron. *Geochim. Cosmochim Acta* **51**, 1561–1571 (1987).
23. Percak-Dennett, E. et al. Microbial acceleration of aerobic pyrite oxidation at circumneutral pH. *Geobiology* **15**, 690–703 (2017).
24. Ghosh, W. & Dam, B. Biochemistry and molecular biology of lithotrophic sulfur oxidation by taxonomically and ecologically diverse bacteria and archaea. *Fems Microbiol. Rev.* **33**, 999–1043 (2009).
25. Kodama, Y. & Watanabe, K. Sulfuricurvum kujiense gen. nov., sp. nov., a facultatively anaerobic, chemolithoautotrophic, sulfur-oxidizing bacterium isolated from an underground crude-oil storage cavity. *Int. J. Syst. Evol. Micr.* **54**, 2297–2300 (2004).
26. Chang, C. T. et al. Shifts in stream hydrochemistry in responses to typhoon and non-typhoon precipitation. *Biogeosciences* **15**, 2379–2391 (2018).
27. Meyer, K. J., Carey, A. E. & You, C. F. Typhoon impacts on chemical weathering source provenance of a high standing island watershed, Taiwan. *Geochim. Cosmochim Acta* **215**, 404–420 (2017).
28. Turowski, J. M. et al. Distribution of erosion across bedrock channels. *Earth Surf. Process Landf* **33**, 353–363 (2008).
29. Hall, F. R. Dissolved solids-discharge relationships: 1. Mixing models. *Water Resour. Res.* **6**, 845–850 (1970).
30. Knapp, J. L. et al. Concentration–discharge relationships vary among hydrological events, reflecting differences in event characteristics. *Hydrol. Earth Syst. Sci.* **24**, 2561–2576 (2020).
31. Shi, L. et al. Extracellular electron transfer mechanisms between microorganisms and minerals. *Nat. Rev. Microbiol* **14**, 651–662 (2016).
32. Magnabosco, C. et al. The biomass and biodiversity of the continental subsurface. *Nat. Geosci.* **11**, 707–717 (2018).
33. Gu, X., Heaney, P. J., Reis, F. D. A. A. & Brantley, S. L. Deep abiotic weathering of pyrite. *Science* **370**, eabb8092 (2020).
34. Hilton, R. G., Gaillardet, J., Calmels, D. & Birck, J. L. Geological respiration of a mountain belt revealed by the trace element rhenium. *Earth Planet. Sci. Lett.* **403**, 27–36 (2014).
35. Hemingway, J. D. et al. Microbial oxidation of lithospheric organic carbon in rapidly eroding tropical mountain soils. *Science* **360**, 209–212 (2018).
36. Hilton, R. G. et al. Climatic and geomorphic controls on the erosion of terrestrial biomass from subtropical mountain forest. *Global Biogeochem. Cy.* **26**, GB3014 (2012).
37. Soulet, G. et al. Temperature control on CO_2 emissions from the weathering of sedimentary rocks. *Nat. Geosci.* **14**, 665–671 (2021).
38. Lyons, W. B., Nezat, C. A., Carey, A. E. & Hicks, D. M. Organic carbon fluxes to the ocean from high-standing islands. *Geology* **30**, 443–446 (2002).
39. Teng, L. S. Geotectonic evolution of late Cenozoic arc-continent collision in Taiwan. *Tectonophysics* **183**, 57–76 (1990).
40. Yanites, B. J. et al. Incision and channel morphology across active structures along the Peikang River, central Taiwan: Implications for the importance of channel width. *Geol. Soc. Am. Bull.* **122**, 1192–1208 (2010).
41. Simoes, M. et al. Mountain building in Taiwan: A thermokinematic model. *J. Geophys. Res. Solid Earth* **112**, B11405 (2007).
42. Beyssac, O. et al. Late Cenozoic metamorphic evolution and exhumation of Taiwan. *Tectonics* **26**, TC6001 (2007).
43. Stanley, R. S., Hill, L. B., Chang, H. C. & Hu, H. N. A transect through the metamorphic core of the Central Mountains, southern Taiwan. *Mem. Geol. Soc. China* **4**, 443–473 (1981).
44. Keyser, W. et al. High-pressure metamorphism in the Chinshuichi area, Yuli belt, eastern Taiwan. *Tectonophysics* **692**, 191–202 (2016).
45. Yui, T.-F. & Lo, C.-H. High-pressure metamorphosed ophiolitic rocks from the Wanjung area. *Taiwan. Proc. Geol. Soc. China* **32**, 47–62 (1989).
46. Baziotis, I. et al. New P–T constraints on the Tamayen glaucophane-bearing rocks, eastern Taiwan: Perple_X modelling results and geodynamic implications. *J. Metamorph. Geol.* **35**, 35–54 (2017).
47. Yui, T. et al. Subduction-related 200 Ma Talun metagranite, SE Taiwan: An age constraint for palaeo-Pacific plate subduction beneath South China Block during the Mesozoic. *Int. Geol. Rev.* **59**, 333–346 (2017).
48. Parada, A. E., Needham, D. M. & Fuhrman, J. A. Every base matters: assessing small subunit rRNA primers for marine microbiomes with mock communities, time series and global field samples. *Environ. Microbiol.* **18**, 1403–1414 (2016).
49. Tu, T.-H. et al. The biogeographic pattern of microbial communities inhabiting terrestrial mud volcanoes across the Eurasian continent. *Biogeosciences* **19**, 831–843 (2022).
50. Tu, T.-H. et al. Microbial community composition and functional capacity in a terrestrial ferruginous, sulfate-depleted mud volcano. *Front. Microbiol.* **8**, 2137 (2017).
51. Wang, P.-L. et al. Spatial variations of community structures and methane cycling across a transect of Lei-Gong-Hou mud volcanoes in eastern Taiwan. *Front. Microbiol.* **5**, 2946 (2014).
52. Alm, E. W. et al. The oligonucleotide probe database. *Appl. Environ. Microbiol.* **62**, 3557–3559 (1996).
53. Schloss, P. D. et al. Introducing mothur: open-source, platform-independent, community-supported software for describing and comparing microbial communities. *Appl. Environ. Microbiol.* **75**, 7537–7541 (2009).
54. Bolyen, E. et al. Reproducible, interactive, scalable and extensible microbiome data science using QIIME 2. *Nat. Biotechnol.* **37**, 852–857 (2019).
55. Callahan, B. J. et al. DADA2: High-resolution sample inference from Illumina amplicon data. *Nat. Methods* **13**, 581–583 (2016).
56. Quast, C. et al. The SILVA ribosomal RNA gene database project: improved data processing and web-based tools. *Nucleic Acids Res.* **41**, D590–D596 (2013).
57. Li, D. H. et al. MEGAHIT: an ultra-fast single-node solution for large and complex metagenomics assembly via succinct de Bruijn graph. *Bioinformatics* **31**, 1674–1676 (2015).
58. Kang, D. W. D. et al. MetaBAT 2: an adaptive binning algorithm for robust and efficient genome reconstruction from metagenome assemblies. *Peerj* **7**, e7359 (2019).
59. Wu, Y. W. et al. MaxBin: an automated binning method to recover individual genomes from metagenomes using an expectation-maximization algorithm. *Microbiome* **2**, 26 (2014).
60. Alneberg, J. et al. Binning metagenomic contigs by coverage and composition. *Nat. Methods* **11**, 1144–1146 (2014).
61. Uritskiy, G. V., DiRuggiero, J. & Taylor, J. MetaWRAP—a flexible pipeline for genome-resolved metagenomic data analysis. *Microbiome* **6**, 158 (2018).
62. Parks, D. H. et al. CheckM: assessing the quality of microbial genomes recovered from isolates, single cells, and metagenomes. *Genome Res.* **25**, 1043–1055 (2015).
63. Chaumeil, P.-A., Mussig, A. J., Hugenholtz, P. & Parks, D. H. GTDB-Tk: a toolkit to classify genomes with the Genome Taxonomy Database. *Bioinformatics* **36**, 1925–1927 (2019).
64. Hyatt, D. et al. Prodigal: prokaryotic gene recognition and translation initiation site identification. *BMC Bioinformatics* **11**, 119 (2010).
65. Seemann, T. Prokka: rapid prokaryotic genome annotation. *Bioinformatics* **30**, 2068–2069 (2014).
66. Patro, R. et al. Salmon provides fast and bias-aware quantification of transcript expression. *Nat. Methods* **14**, 417–419 (2017).

67. Markowitz, V. M. et al. IMG: the integrated microbial genomes database and comparative analysis system. *Nucleic Acids Res.* **40**, D115–D122 (2012).
68. Langmead, B. & Salzberg, S. L. Fast gapped-read alignment with Bowtie 2. *Nat. Methods* **9**, 357–359 (2012).
69. Kanehisa, M. & Goto, S. KEGG: Kyoto Encyclopedia of Genes and Genomes. *Nucleic Acids Res.* **28**, 27–30 (2000).
70. Kanehisa, M. et al. KEGG for integration and interpretation of large-scale molecular data sets. *Nucleic Acids Res* **40**, D109–D114 (2012).
71. Hopkinson, B. M. & Barbeau, K. A. Iron transporters in marine prokaryotic genomes and metagenomes: Iron transporters in marine prokaryotes. *Environ. Microbiol.* **14**, 114–128 (2011).
72. Reveillaud, J. et al. Subseafloor microbial communities in hydrogen-rich vent fluids from hydrothermal systems along the Mid-Cayman Rise. *Environ. Microbiol.* **18**, 1970–1987 (2016).
73. Galambos, D., Anderson, R. E., Reveillaud, J. & Huber, J. A. Genome-resolved metagenomics and metatranscriptomics reveal niche differentiation in functionally redundant microbial communities at deep-sea hydrothermal vents. *Environ. Microbiol.* **21**, 4395–4410 (2019).
74. Chao, A. Estimating the population-size for capture recapture data with unequal catchability. *Biometrics* **43**, 783–791 (1987).
75. Shannon, C. E. & Weaver, W. *The Mathematical Theory of Communication* (University of Illinois, 1949).
76. Chao, A., Chazdon, R. L., Colwell, R. K. & Shen, T. J. A new statistical approach for assessing similarity of species composition with incidence and abundance data. *Ecol. Lett.* **8**, 148–159 (2005).
77. Paulson, J. N., Stine, O. C., Bravo, H. C. & Pop, M. Differential abundance analysis for microbial marker-gene surveys. *Nat. Methods* **10**, 1200–1202 (2013).
78. Bray, J. R. & Curtis, J. T. An ordination of the upland forest communities of southern Wisconsin. *Ecol. Monogr.* **27**, 325–349 (1957).
79. Anderson, M. & Braak, C. T. Permutation tests for multi-factorial analysis of variance. *J. Stat. Comput. Sim.* **73**, 85–113 (2003).
80. Wickham, H. *ggplot2, Elegant Graphics for Data Analysis*, https://doi.org/10.1007/978-3-319-24277-4_7 (Springer-Verlag, 2016).
81. McMurdie, P. J. & Holmes, S. phyloseq: an R package for reproducible interactive analysis and graphics of microbiome census data. *Plos One* **8**, e61217 (2013).
82. Dixon, P. VEGAN, a package of R functions for community ecology. *J. Veg. Sci.* **14**, 927–930 (2003).
83. Bastian, M., Heymann, S. & Jacomy, M. Gephi: an open source software for exploring and manipulating networks. In *Third International AAAI Conference on Weblogs and Social Media.* (AAAI Publications; 2009), pp. 361–362.

Acknowledgements

We appreciate the invaluable comments and suggestions provided by three reviewers. We are grateful to the funding support from Taiwanese MOE and NSTC (MOST) to PLW (MOST 110-2116-M-002-006-MY3), YMW (MOE 110L9010), THT (NSTC 112-2116-M-110-002), and LHL (NSTC 112-2116-M-002-010). We also acknowledge the logistical support and comments provided by Sun-Lin Chung and Ching-Hua Lo, and the assistance in sampling and geochemical analyses by Ya-Fang Cheng, Yueh-Ting Lin, I-Feng Wu, Ruei-Feng Tsai, Bo-Yu Chen, Jing-Yi Tseng, and Ling-Wen Liu.

Author contributions

P.L.W. and L.H.L. conceived the study design and coordinated the project. P.L.W., T.H.T. and L.H.L. co-wrote the initial draft and contributed equally to this work. P.L.W., T.H.T., L.H.L., H.L.C., L.Y.W., J.N.C. and J.M.C. performed the sampling. P.L.W., T.H.T., L.H.L., Y.J.W., J.N.C., L.Y.W., M.F.C., C.F.C, Y.C.H. and C.P.C. performed data analysis and processing. P.L.W., T.H.T., L.H.L., Y.J.W., J.N.C., Y.M.W., Y.T.L. and C.C.K. conducted data compilation and interpretation and commented on and revised the manuscript.

Competing interests

The authors declare no competing interests.

Additional information

Supplementary information The online version contains supplementary material available at https://doi.org/10.1038/s43247-024-01345-3.

Correspondence and requests for materials should be addressed to Pei-Ling Wang or Tzu-Hsuan Tu.

Peer review information *Communications Earth & Environment* thanks Niels Hovius and the other, anonymous, reviewer(s) for their contribution to the peer review of this work. Primary Handling Editors: Xiao-Ming Liu and Clare Davis. A peer review file is available.